

This item is the archived peer-reviewed author-version of:
Three-dimensional electron microscopy of chiral nanoparticles : from imaging to measuring
Reference: Girod Robin, Vlasov Evgenii, Liz-Marzan Luis M., Bals Sara Three-dimensional electron microscopy of chiral nanoparticles: from imaging to measuring Nano letters / American Chemical Society - ISSN 1530-6992 - Washington, Amer chemical soc, 25:19(2025), p. 7629-7640 Full text (Publisher's DOI): https://doi.org/10.1021/ACS.NANOLETT.5C01640 To cite this reference: https://hdl.handle.net/10067/2145690151162165141

uantwerpen.be

Three-dimensional electron microscopy of chiral nanoparticles: from imaging to measuring

Robin Girod¹, Evgenii Vlasov¹, Luis M. Liz-Marzan^{2,3,4,5} and Sara Bals^{1,*}

¹ EMAT and NANOlight Center of Excellence, University of Antwerp, Groenenborgerlaan 171, Antwerp B-2020, Belgium

² CIC biomaGUNE, Basque Research and Technology Alliance (BRTA), 20014 Donostia-San Sebastián, Spain

³ Ikerbasque, Basque Foundation for Science, 48009 Bilbao, Spain

⁴ Centro de Investigación Biomédica en Red, Bioingeniería, Biomateriales y Nanomedicina (CIBER-BBN), 20014 Donostia-San Sebastián, Spain

⁵CINBIO, University of Vigo, 36310 Vigo, Spain

* Email: sara.bals@uantwerpen.be

KEYWORDS

Electron tomography, secondary electron imaging, three-dimensional microscopy, chirality, plasmonic nanoparticles

ABSTRACT

The increasing interest on plasmonic nanoparticles with intrinsic chirality, i.e., reduced symmetry and strong optical activity, calls for characterization beyond qualitative imaging. In this context, three-dimensional electron microscopy (3D EM), which provides images containing information on the particles' surface and may even retrieve the explicit 3D shapes, is seeing exciting developments and applications. In this Mini Review, we focus on scanning electron microscopy (SEM), electron tomography, and secondary electron electron-beam induced current (SEEBIC). We highlight the recent advances in these 3D EM techniques and in the analysis of their data that relate to chiral metallic nanoparticles. The study of shape-properties relationships, in particular by quantitatively analyzing geometric chirality and informing electromagnetic simulations, is covered. New ways 3D characterization is revealing the growth pathways of the nanoparticles are also presented. Finally, we provide an outlook into future opportunities for 3D EM to further guide the understanding and development of (chiral) nanoparticles.

1. Introduction

The insights offered by characterization at high spatial resolution has long established electron microscopy (EM) as a cornerstone of nanosciences. Shapes and morphology can be imaged with high-throughput in scanning electron microscopes (SEM), while state-of-the-art aberration-corrected (scanning) transmission electron microscopes (STEM) offer a range of analyses including characterization of the morphology, structure, composition, electromagnetic properties, and more.¹

Motivated by the development of nanoparticles with growing complexity, ^{2,3} the conventional 2D images have been increasingly complemented by characterization in 3D.⁴⁻⁶ In EM, two strategies can be employed to access 3D information; topographic information can be encoded into images through surface imaging, or 3D data can be explicitly retrieved using 2D images acquired from different viewing directions.⁷ SEM is the most well-known representative of the former approach, and offers high throughput and ease of use but limited spatial resolution. On the other hand, 3D methods leveraging the atomic resolution of STEMs and modern computational capabilities have seen increasing development and application. Electron tomography, which computationally retrieves the full 3D geometry of the specimen from a tilt series of 2D projections, is currently available in many research labs.^{5,6,8} In addition, surface imaging in STEMs with secondary electron (SE) detectors, or the recently introduced SE electron beam induced current (SEEBIC) method, enable high throughput while maintaining a good signal-to-noise ratio, thus holding promise for the characterization of complex nanomaterials.^{9,10}

The motivation for 3D EMs is perhaps nowhere as apparent as in the rapidly developing field of chiral inorganic nanoparticles.^{11–13} Towards applications that include biosensing, therapeutics and catalysis, materials that exhibit surface plasmon resonances, such as gold and silver, can be now made into nanoparticles with intrinsic chirality.^{12,14} The library of shapes is expanding quickly, ranging from a variety of twisted morphologies to more complex shapes for which handedness is not immediately apparent.^{15,16} As the chirality of these shapes is most often only perceptible in 3D, the inspection of the synthesis product with SEM or ET has become routine, revealing for example the complex morphologies of helicoids with 432 symmetry or of nanorods with nm-sized, helical, wrinkles.^{2,17}

Furthermore, 3D characterization is key to understand the intricate optical-structural relationships in chiroptical nanoparticles. The excitation of surface plasmons on chiral metal nanoparticles indeed results in the very strong differential extinction of right- and left-handed polarized light, as measured by anisotropy factors (*g*-factors) orders of magnitude higher than those of chiral molecules.^{2,17,18} The structural origins of this behavior remain poorly understood but are key to tailor particles to specific applications. To this end, quantitative shape descriptors have been developed to capture some aspects of chirality and predict optical

asymmetry.^{19–21} In addition, electron tomography reconstructions can serve as input models for electromagnetic modeling of surface plasmons, or enable their 3D measurement when combined with electron energy loss spectroscopy (EELS), thereby achieving direct visual correlations between experiments and optical modes.^{22,23}

Finally, 3D EM is also relevant to progress towards accurate and predictable syntheses of chiral particles with specific shapes. ¹² At present, the fabrication of these particles typically involves chemical growth onto achiral seeds, in the presence of molecular chirality inducers. This transfer of chirality from molecules to inorganic nanomaterials is now well documented for molecular inducers like helical micelles^{2,24} or smaller amino acids and related molecules, ^{12,17,18} and for external stimuli, such as circularly polarized light (CPL). ¹⁵ Yet, the synthetic toolbox is far from being entirely explored and the mechanisms of chirality transfer remain to be fully understood. Here, 3D EM, in combination with tailored experimental plans and adequate data analysis, can follow the evolution of nanoparticles at various stages of growth, provide mechanistic insights, and inform about optical, geometrical and structural transitions. ^{18,25,26}

In view of the recent advances in both chiral inorganic nanostructures and 3D EM, a Mini-Review of the progress beyond the simple qualitative imaging of synthesis products appears timely. We start with a brief introduction to the relevant 3D EMs, based on either SEM or STEM (**Figure 1**, inner ring). We then present the main avenues through which 3D EM and related data analysis can contribute to better understand and eventually apply inorganic chiral nanostructures (**Figure 1**, outer ring). For each, we highlight selected examples that demonstrate the interest of 3D characterization. Specifically, we consider the study of structure-property relationships, which can be qualitative, relying on the unambiguous visualization of the chiral morphologies, and quantitative, through the design and use of chirality measures extracted from 3D EM data sets. Special attention is devoted to the high throughput required to ensure statistically relevant analysis. Since the comprehension of relevant growth mechanisms is crucial to the realization of desired geometries, we then focus on 3D EM-enabled methods for mechanistic studies of chiral growth. The final section offers an outlook on the future of 3D EM, highlighting the potential to further guide the understanding and development of chiral synthesis for controlled shapes and predefined chiroptical properties.

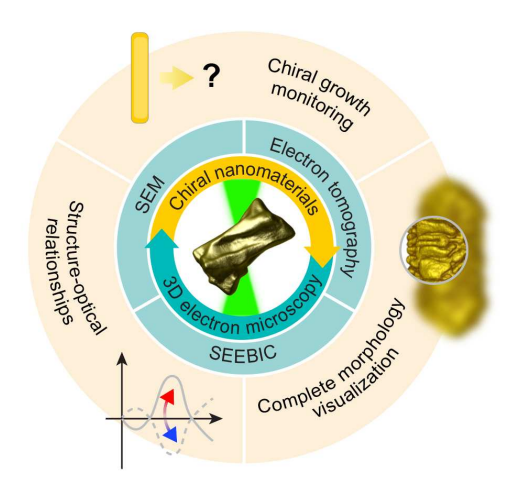


Figure 1: Imaging methods (green) and typical applications (yellow) of 3D electron microscopy for chiral nanoparticles.

2. State of the art methods for 3D characterization of chiral NPs

We first introduce (**Figure 2**) and compare (**Table 1**) the 3D EM methods that are most commonly used to characterize the morphology of (chiral) nanomaterials, namely SEM and electron tomography. In addition, we describe SEEBIC, a recently proposed imaging method that enables surface-like imaging in a STEM, thus combining high throughput and high spatial resolution.

SEM is undoubtedly the most straightforward approach to obtain 3D information of nanomaterials, as topographic contrast is readily obtained, most commonly through SE imaging. SEs are generated upon inelastic collision of the primary electron beam with the specimen. Because of their low energy ($\leq 50 \text{ eV}$), only those generated in close vicinity to the surface (< 5 nm in metals) will escape from the sample and reach a detector (e.g. scintillator-photomultiplier) to contribute to the formation of an image (Figure 2a).²⁷ In addition, the SE detector is usually positioned on the side of the imaging area, which creates a shadowing effect and highlights the topography of the sample. The low acceleration voltage (typically 2-30 kV) of the electron gun and aberrations of the electromagnetic lenses determine the spatial resolution, which is typically ~1 nm at best. Nonetheless, the ease-of-use, large field of view and fast acquisition time often make SEM the most appropriate choice for 3D characterization by EM, especially for relatively large nanoparticles.¹⁷ While SEM images only provide a pseudo-3D perception of the object, the nature of the topographic contrast makes them suitable to a range of photogrammetry techniques for explicit retrieval of the full 3D morphology.²⁸ In these approaches, images at various orientations are acquired and the corresponding camera positions are calibrated in space. Computed algorithms are available to then reconstruct a surface mesh corresponding to the recorded images.²⁸ High level of detail can be obtained but the achievable resolution remains inherently constrained by the SEM imaging capabilities.²⁹ Furthermore,

only the visible surface can be reconstructed because limited information is available from the interior of the specimen or the faces in contact with the support.

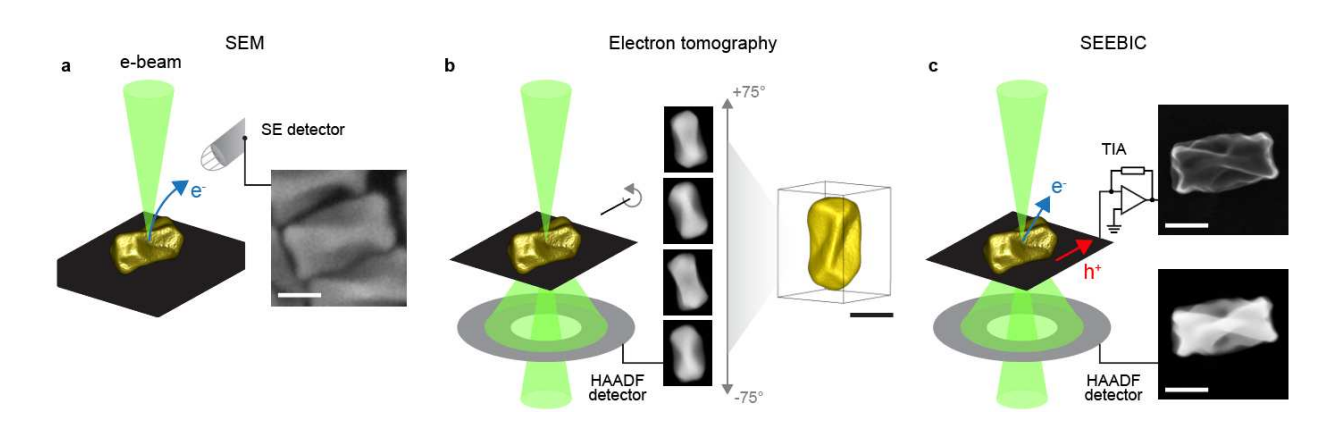


Figure 2: Methods for 3D imaging. (a) principle of SEM. Image adapted with permission from ref ³⁰. Copyright 2024, John Wiley and Sons. (b) Principle of electron tomography in HAADF-STEM mode. (c) principle of SEEBIC. Scale bars are 50 nm.

Table 1: Comparison of the characteristics of SEM, SEEBIC, and electron tomography. Abbreviations: CL, cathodoluminescence; EDS, energy dispersive spectroscopy; EELS, electron energy loss spectroscopy; 4D-STEM, four-dimensional STEM; 3D-ED, 3D electron diffraction.

	SEM		Electron tomography		SEEBIC	
Acquisition time	< 1 min		20 – 60 min Down to 5 min in fast tomography mode	9,31 6,32	1 - 5 min	9,10
Required electron dose	$1 - 10^3 \text{ e}^{-1}/\text{Å}^2$	27	$10^4 - 10^6 \text{ e}^{-1}/\text{Å}^2$	31	$10^3 - 10^5 \text{ e}^{-}/\text{Å}^2$	9,10
Spatial resolution	nm	27	Å	18,33–35	Å	9,10
Explicit 3D reconstruction	Partial	28,29,36,37	Yes	21,30,38	Under development	10
Complementary techniques	Established: low-resolution STEM-in-SEM, <i>in situ</i> methods, CL		Established: EDS, EELS, 4D-STEM, 3D-ED, liquid phase, CL In development: heating in situ	5,24,39 6,32,34,40	Established: HAADF In development: heating <i>in situ</i> Feasible: EDS, EELS, 4D-STEM, CL	

On the other hand, (S)TEM employs higher acceleration voltages (typically 60-300 kV) than SEM and, in many modern instruments, aberration correctors are used to focus a sub-nm electron probe on the sample, routinely resulting in images with atomic resolution. High angle annular dark field (HAADF) detectors, which collect transmitted electrons scattered in Rutherford-like events, yield images with mass-thickness contrast in which the intensity scales with $\sim tZ^{1.7}$, where t is the material thickness and Z the atomic number. HAADF-STEM images can therefore be considered as true projections of the object, making them suitable for tomographic reconstruction. Tomography aims at inverting the projection transform to

retrieve the original object. 442 In practice, the procedure amounts to finding a 3D volume that is consistent with the experimentally acquired images. HAADF-STEM images at various viewing angles are first acquired by tilting the sample (**Figure 2b**), and the resulting tilt series are then used to compute a voxelated volume. Numerous algorithms have been developed for this purpose, and can nowadays incorporate prior knowledge about the specimen 43-45 or the image formation process 46,47 to provide high quality 3D reconstructions. The data can subsequently be inspected, e.g., by slicing through the 3D volume to visualize tomograms, or by rendering the surface (**Figure 2b**). On dispersed metallic nanoparticles, nm-sized features are routinely resolved, while atomic-resolution electron tomography enabled by advanced reconstruction procedures is becoming increasingly common. 35,48

Furthermore, the recent developments of multimode and fast electron tomography have expanded the field of application of the technique. In multimode tomography, different signals can be acquired simultaneously and their corresponding 3D information can be reconstructed together (**Table 1**). For example, 3D chemical maps can be computed from energy dispersive spectroscopy (EDS) or electron energy loss spectroscopy (EELS) data sets. 49,50 This allows clearer visualization and analysis in multielement systems, such as alloy chiral nanocatalysts or core-shell plasmonic particles 5,51 EELS also enables plasmon imaging which can be of particular interest for chiroptical nanoparticles (see **Section 3**). Moreover, tilt-series of diffraction patterns can be acquired to simultaneously reconstruct the reciprocal lattice in 3D electron diffraction (3D-ED). An application of this approach is highlighted in **Section 4**. For additional details, comprehensive presentations of multimode tomography have been proposed by the groups of Bals and Midgley. Midgley.

Tilt series acquisitions typically comprise 30-80 images acquired over the course of 30-60 minutes, making conventional electron tomography a low-throughput, electron-dose intensive technique. This not only poses a challenge to sensitive samples, but also limits the statistical significance on polydisperse materials. To accelerate the acquisition procedure, fast approaches typically involve the automation of the tilting process, continuous image acquisition, and selection of undistorted projections during post-processing.^{6,54,55} In this manner, a tilt-series can be collected within minutes. Fast tomography has also enabled to track dynamic processes in 3D, such as the reshaping of plasmonic particles upon heating, which is relevant towards their application in photothermal therapy or catalysis.^{6,32,55,56}

It should be noted that the quality of a tomographic reconstruction largely depends on acquisition parameters such as the angular increment and the choice and optimization of the reconstruction algorithms. In addition, post-processing steps to align the projections are critical prior to the reconstruction, dedicated grids and holders are necessary to ensure high-tilt range, and, except on the most stable metallic materials, the electron dose needs to be controlled to avoid beam-induced damage.⁵⁷ Electron tomography therefore

remains an advanced microscopy technique with important user involvement. Readers interested in the more practical aspects of the method will benefit from comprehensive resources available elsewhere.^{53,58}

Alternatively, SE imaging can be realized in STEM instruments by integrating a dedicated detector in the vicinity of the specimen.⁵⁹ While the signal generation process is similar to that in SEM, the geometry of the STEM electromagnetic lenses poses technical challenges to this implementation and limits the collection of SEs, making SE detectors noisy and rarely available in commercial instruments. To overcome these limitations, Vlasov et al. recently proposed the use of SE-electron beam induced current (SEEBIC) imaging for the 3D characterization of nanoparticles. 9,10 Instead of capturing the SEs, this approach uses the holes that are created by the escaping electrons. At each e-beam position, the emission of SEs creates a potential in the material and a current of positive charges that is proportional to the number of emitted SEs. This current can be measured with an adapted holder, amplified, and translated into image intensities (Figure 2c). Similar to SEM images, a topographical perception of the surface arises due to the dependence of the SE yield on surface orientation relative to incident electron beam, the directional dependence of SE yield, and the "edge effect". ²⁷ Even atomic resolution can be obtained, ⁶⁰ and hundreds of particles per experiment can be imaged with doses comparable to those in conventional electron tomography, but with gains in acquisition speed of 1-2 orders of magnitude. 10 Importantly, SEEBIC and HAADF imaging can be achieved simultaneously, thus providing information not only about the surface but also about the projected specimen thickness. This technique is readily compatible with compositional analysis and plasmon mode visualization in EELS or cathodoluminescence (CL), combinations that are of particular interest for the study of optical materials. Although still a confidential method, SEEBIC is set to become more widely available owing to its unique benefits for 3D nanocharacterization and promised ease of implementation. In the following, we detail how these 3D EM methods can support the understanding and optimization of structure-property connections and the growth of chiral nanoparticles.

3. 3D EM to understand shape-optical relationships in chiral nanoparticles

3.1. Qualitative relationships from morphology visualization

The complex shapes of chiral nanoparticles can hardly be predicted from ensemble measurements, which hampers a clear understanding of the origin of their optical response. For example, clarifying trends in the strength of differential extinction under illumination with right- and left-handed CPL, wavelength shifts in circular dichroism peak(s), and understanding the CD sign, are important to enable the predictable production of particles with the desired properties. Therefore, the first application of 3D EM often lies in the accurate visualization of the nanostructures from which a chiroptical signal arises. If the particles assume

a shape with a clearly defined handedness, e.g., a twisted or helical one, SEM, SEEBIC, or electron tomography will directly enable its identification (**Figure 2**), and the correlation between geometrical and optical handedness may be evident, as was shown for bowtie assemblies, ¹⁹ twisted nanorods, ¹⁸ or mature helicoid III particles. ¹⁷ However, many chiral particles show strong optical activity without clearly defined geometrical handedness. This can be due to the lack of a well-defined shape, for instance in CPL-induced nanostructures; ¹⁵ intra- and inter-particle polydispersity, for example in wrinkled gold nanorods; ² or because of the presence of multiple chiral centers, as found again in wrinkled nanorods or in bichiral helicoids with 432 symmetry. ⁶¹ To understand and optimize the shape-optical relationships in such particles, quantitative descriptors of chirality, possibly at different length scales, are required.

3.2. Chirality measures for quantitative 3D analysis

Quantitative shape descriptors can be broadly categorized by their end-goal, which we classify here as relating to *explaining* and/or *predicting* a given optical property or trend. To explain the origin of a chiroptical signal, a descriptor needs to be intuitive and relate to interpretable geometrical features.²¹ With this goal in mind, an approach of major interest for 3D EM data is to consider the helical character of a shape and, specifically, to measure the helical inclination of surface features. Here, the helical inclination describes the angle of a surface feature with a plane perpendicular to the helical axis. As initially proposed Heyvaert *et al.*, the measure operates on rod-like nanostructures, from which a triangulated surface mesh or a voxelated 3D data set first needs to be obtained, typically using electron tomography.²¹ Next, the inclination can be computed by using the Euler angles of the surface normals,^{25,30,38} or image gradients.^{10,18,21} The computed inclination can be visualized (**Figure 3a**), and statistically evaluated.^{25,30} It has been shown, for example, that the inclination angle of surface features in wrinkled particles often oscillates in periodic patterns (**Figure 3b**),³⁰ and that a lower inclination variance, indicative of higher feature alignment, correlates with higher g-factors in wrinkled helical particles.²⁵

Building on the definition of the helical inclination, a helicity measure was proposed by Heyvaert *et al.* This measure is intimately connected to the inclination and is defined as the integral of the sign of the inclination over a surface, normalized to the surface area.²¹ More intuitively, it can be shown that the helicity describes the difference between the fraction of a given surface that has positive inclination (i.e., is right-handed) and the fraction that has negative inclination (i.e., is left-handed).²⁵ This yields a (pseudo-scalar) metric, termed *total* helicity when applied to an entire particle or *local* helicity when calculated within a sub-area of a mesh (**Figure 3c**). By definition, a perfect right-handed helix possesses a total helicity of +1, respectively -1 for a left-handed one. Thus, the total helicity also describes how close to being perfectly helical a given shape is. For helical and rod-like geometries, the sign of the total helicity is closely connected to the sign of the peak CD signal in the visible and near-infrared range, and its magnitude shows a monotonic relationship

with the value of the peak *g*-factor (**Figure 3d**). The measure has been used to determine the geometrical handedness of complex wrinkled nanoparticles.²¹ Combining electron tomography, helicity analysis, and single particle optical measurements has enabled the correlation of the optical properties of selected particles with their shape.^{38,51} Helicity has also been used to confirm that surface features of opposite handedness were obtained when using nanorod seeds with penta-twinned structure instead of single-crystalline ones, even if the same enantiomer of a chirality inducer was used,³⁰ both for the final product and for intermediate stages during chiral growth.²⁵ In this manner, it was demonstrated that helicity and optical activity decrease during the later stages of growth, indicating that factors affecting helicity, such as the proportion of inclined features or the length and spacing of wrinkles, strongly influence the optical activity.

A second set of explainable descriptors are focused on the concept of asymmetry. Two measures are notable and originate in early attempts to quantify the chirality of organic molecules:⁶² the Hausdorff chirality measure (HCM) aims at calculating the difference between a given shape and its mirror image; whereas the continuous chirality measure (CCM), relies on the distance between a chiral shape and the nearest achiral one obtained by continuously deforming the starting geometry. Both approaches are computationally demanding because they require optimizing the spatial alignment of two shapes to ensure that the measured difference reflects true asymmetry rather than misalignment.⁶³ In addition, the Hausdorff distance is relevant to simple shapes, consisting of a few datapoints, like molecules, but it is time consuming for complex geometries such as nanoparticle surfaces reconstructed by electron tomography. A strategy proposed by Kotov et al. is to divide the shape of interest in octants and calculate the Hausdorff distance using the centerof-mass of each sub-volumes, that is, to coarse-grain the structure. 15,64 Although this speeds up the calculation, subtle surface features of the particle that might be important are lost in the process. Another alternative proposes replacing the Hausdorff distance with the disjunctive union between a binarized reconstruction and its mirror image. 65 The disjunctive union is the non-overlapping volume between two shapes (red in Figure 3e), so that normalizing it to the total volume of a particle (red and white in Figure 3e) yields an asymmetry measure (AM, Figure 3f). Visualization allows to appreciate the localization and importance of the non-overlapping, i.e., asymmetric areas (Figure 3e). The required minimization can be completed within minutes for volumes of $\sim 150^3$ voxels and is therefore tractable on detailed tomography reconstructions of chiral nanoparticles. It should be noted that all measures related to asymmetry are unsigned and therefore do not provide information about the handedness. Nonetheless, within given shape families such as helicoid particles with 432 symmetry or helical nanorods, the AM appears to correlate with the absolute magnitude of the peak g-factor (Figure 3f).⁶⁵

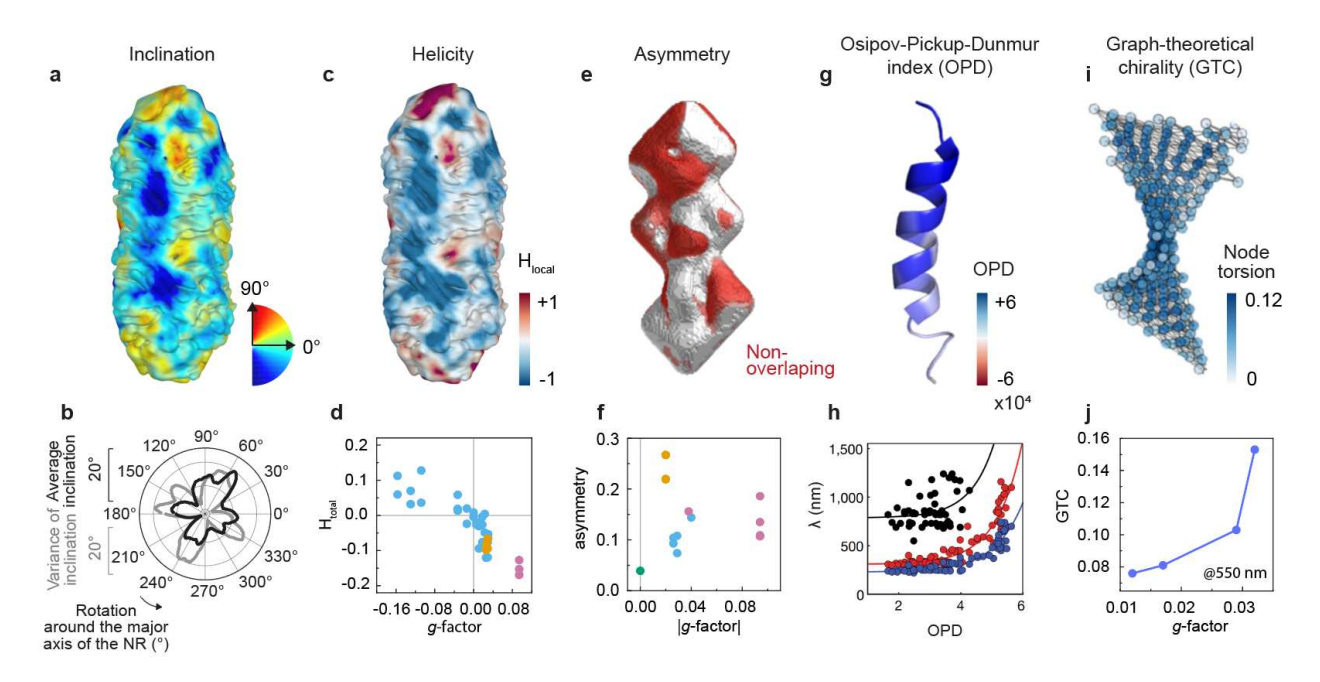


Figure 3: Visual (top) and quantitative (bottom) aspects of chirality-related descriptors from electron tomography reconstructions and 3D models. (a) Surface rendering of the inclination of the surface of a wrinkled particle synthesized with micelle-templated seeded growth on penta-twinned nanorods.³⁰ (b) Mean and variance of the inclination as a function of the position around the major axis of the particle in (a). The calculation was performed in 1° steps and within a 10° window spanning the length of the rod. (c) Local helicity mapping obtained by integrating the sign of the helical inclination in a 4 nm window around each surface point. A positive local helicity indicates a right-handed surface, a negative local helicity indicates a left-handed surface. (d) Variation of total helicity as a function of the peak g-factor for a range of (blue) wrinkled25 and (pink) twisted single-crystalline particles,18,30 and (orange) amino-acid-directed growth product on penta-twinned seeds.³⁰ Adapted with permission from ref ²⁵. Copyright 2025, American Chemical Society. (e) Surface rendering of the asymmetry calculation results. The particle was mirrored, and its position and angle was adjusted with a combination of grid-search and Nealder-Mead optimization until the disjunctive union between the two volume was minimized. The rendering shows non-overlapping areas in red, overlapping ones in white. (f) Variation of asymmetry as a function of the peak g-factor for a range of particles. The color code is identical to (d), with an additional achiral particle (green).⁶⁶ It is clear that non-helical particles (orange) deviate from the trend. (g) Visualization of the N-nearest OPD index on the α -helix 5KHB, chain A, with N = 7. Reproduced with permission from ref ⁶⁷. Copyright 2022, Springer Nature. (h) Wavelength of three CD peaks of photonically active bowties with varying pitch, length, width and thickness OPD index, as a function of their OPD index. A correlation is seen between the positions of the peaks and the OPD index of the particles. Reproduced with permission from ref ¹⁹. Copyright 2023, Springer Nature. (i) Visualization of the node torsion in the graph of a twisted ribbon of chiral gold cluster. The GTC index is calculated from the difference in distance and torsion of the nodes on both sides of a semi-mirror plane separating the graph. (j) Variation of GTC as a function of the peak g-factor for simulated helical structures with varying helical pitch. (i, j) are reproduced with permission from ref 68. Copyright 2024, John Wiley and Sons.

The second objective of chirality descriptors is to provide *predictive* power and, thus, optimization capabilities. To this end, the descriptors need to correlate with a given optical property of interest, such as the *g*-factor or the peak wavelength. The descriptors can be less intuitive, insofar as the goal is to predict rather than to explain. Applications would then include using the descriptors as the parameter to be optimized

during geometrical space search, or in feedback loops between characterization, design and synthesis. 14,20,67 Both helicity and asymmetry could be used to that end, for instance to design the most helical nanorod or the helicoid with the highest asymmetry. Other metrics with demonstrated predictive power include the Osipov-Pickup-Dunmur (OPD) index, ⁶⁹ and the graph theoretical chirality (GTC). ⁶⁸ The former was derived by analogy with the theory of optical activity, and relies on point cloud calculations (such as atoms in a molecule) to yield a chirality tensor that encodes the degree of asymmetry in all directions around a given point.⁶⁹ The calculation iterates over all 4-points permutation within a point cloud, and its signed nature relies primarily on the presence of a cross-product that will change sign upon mirroring. The measure is naturally applicable to 3D EM data because the point cloud can be extracted from a triangulated mesh or coarse-grained from electron tomography reconstructions. The index can be mapped for visualization by restricting the calculation to the nearest neighbors of a given point (Figure 3g)^{20,67} or summarized into a single value when all points within a particle are being considered. 16,19 Despite being computationally challenging due to the number of permutations, the OPD has found application as a predictor in various cases: optimization of chiral kirigami, 20 prediction of protein-NP assemblies, 67 demonstration of a chirality continuum based on photonic bowties, 19 and to demonstrate that intricate particles without evident handedness were indeed geometrical enantiomers and triggered different immune responses.¹⁶ Importantly, transition through a chiral zero is not explicitly enforced, which in theory can yield a null OPD index even on chiral shapes.⁷⁰ Different from the OPD approach, the GTC operates on graphs which, here again, can be readily obtained by considering a triangulated surface mesh or coarse graining electron tomography reconstruction. The measure relies on the assumption that asymmetric graphs will exhibit asymmetric torsion, defined as the difference in alternate paths around a graph edge, for instance because of missing nearest neighbors or distorted edges. The asymmetric distribution of the torsion on each side of a semimirror plane enables the calculation of the GTC index. For graphs extracted from 3D structures within a given chirality continuum, for example helical nanostructure (Figure 3i, j), this index can be related to handedness and was shown to scale with properties such as helical pitch, as well as to exhibit a monotonous relationship with the g-factor. 68 The signed nature of the GTC index relies on the position of the semi-mirror plane, which can be found in simple shapes but has to be manually positioned in more complex graphs.⁶⁸

The calculations presented so far operate on explicit 3D data, as typically obtained by electron tomography. However, the throughput of the imaging method is important because chiral nanomaterials may exhibit polydispersity at the inter- or intra-particle level. Wrinkled Au nanorods have for example been shown to feature a mixture of left and right-handed features in varying proportions, so that the dominant handedness needs to be assessed on a sufficient number of particles to be representative of the population. As only a few particles per day can be analyzed with electron tomography, such high throughput and statistical

significance can, at present, only be obtained from surface imaging in SEM or SEEBIC. Thus, a number of dedicated descriptors operating on 2D images have been devised. We have recently proposed an adaptation of the helicity measure, using the directions of the SEEBIC image gradient (Figure 4). Owing to the surfacelike nature of SEEBIC imaging, these directions directly encode information from the orientation of the morphological features. As with 3D data, helical inclination maps can be computed for the visible surface of the particle (Figure 4b). Subsequently, the total helicity (of the visible surface) of the particle (Figure 4c) can be obtained, as previously defined. Helicity plots can also be obtained, showing the contribution of the different inclination angles to the helicity value (Figure 4c). Importantly, the calculation can be performed on hundreds of particles at once, owing to the throughput of SEEBIC, so that an ensemble helicity (H_{ensemble}) can be calculated by averaging the total helicity of many single particles (**Figure 4d**). Initial results suggest a strong association between this SEEBIC-based helicity and g-factor maxima (Figure 4e). Targeting handedness recognition, deep-learning models have been used, e.g. to classify the handedness of CdTe particles. 72,73 This approach relies on the creation of a representative training dataset and the generalization capabilities remain to be investigated. Nonetheless, classification of the handedness of hundreds of particles imaged in SEM has been achieved, providing insights into the distribution of morphologies at the population level.

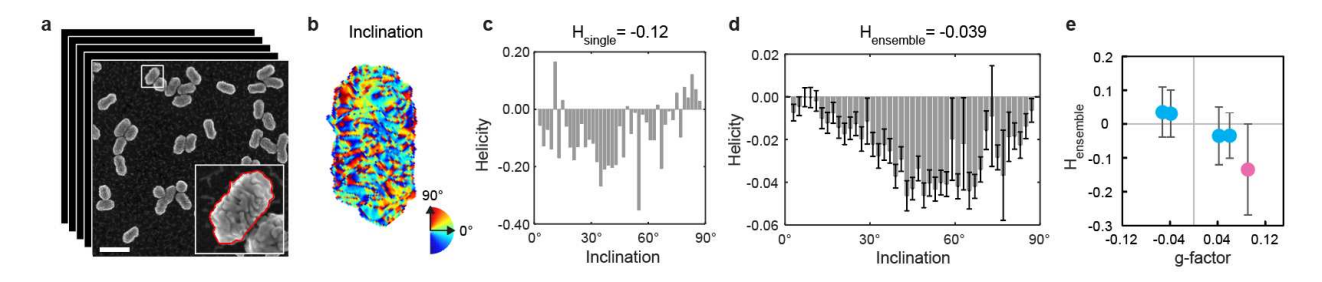


Figure 4: High-throughput quantification of helicity from SEEBIC images. (a) Set of experimental overview SEEBIC images of wrinkled gold nanoparticles. Scale bar is 200 nm. (b) Inclination map obtained for the single nanoparticle in panel (a) and (c), corresponding helicity plot showing the difference in right-handed (positive) and left-handed (negative) surface as a function the absolute inclination angle. (d) Helicity plot for an ensemble of wrinkled gold nanoparticles (N = 348 particles, including the one in (b,c)). Error bars are the standard error for each data bin. (e) Variation of ensemble helicity as a function of the peak *g*-factor for a range of (blue) wrinkled and (pink) twisted particles. Error bars are the standard deviation (N > 100 particles). (a, d) Reproduced with permission from ref 10 . Copyright 2024, American Chemical Society.

It is important to note that, regardless of its goal, a chirality measure is valid only within a selected chirality continuum, i.e., for a given shape family, which intrinsically limits the breadth of the geometric space search based on any given measure. ^{62,74,75} This is mostly because of the well-known problem of chiral zeros, which states that no pseudo-scalar metric can describe the entire chirality space; there must exist a chiral shape

with zero value for the chosen metric.⁷⁰ However, even unsigned metrics can show different relationships with optical properties depending on the shape family (**Figure 3d**). We also note that, chirality can be expressed at multiple scales in both biological and inorganic structures. To capture multiscale chirality it has been useful to define a chirality tensor, for instance by calculating descriptors at different levels of coarse graining.^{19,67}

3.3. 3D plasmon mapping and optical simulations from experimental models

Electromagnetic simulations are widely used to understand how a particle's shape determines its optical properties and to visualize the distribution of electric field enhancement. However, the 3D input to the simulation is often an idealized model, e.g. drawn from SEM images, which may not reflect the complex morphology and polydispersity of chiral products. 3D EM offers two relevant approaches to overcome this problem. First, electron energy loss spectroscopy (EELS) enables direct mapping of plasmon modes excited by an electron beam with a certain energy. Furthermore, when combined with electron tomography in a multimode approach,⁵ the localized surface plasmon resonance components can be reconstructed and analyzed in 3D.²³ The approach has been applied mainly on achiral particles and their assemblies (**Figure 5a**),^{23,76-80} but has also been recently explored to visualize a chiral mode on a gold helicoid nanoparticle (**Figure 5b**).²² It should be noted that the projection requirement for electron tomography should be fulfilled, which poses limitations to the interpretation of EELS tomography for complex shapes.

Therefore, an alternative is to use accurate ET reconstructions as the input for electromagnetic simulations based on the finite-difference time-domain (FDTD) or boundary element methods (BEM). 81,82 In these simulations, a number of considerations will strongly influence the agreement with experiments. In particular, the choice of mesh size will influence the accuracy of the results, but also the computational resources required. The dielectric constant of the environment is important, as is the presence and localization of a substrate. As experiments measure ensemble-average properties, the polydispersity of the sample must also be kept in mind, and averaging of simulations with different direction of light propagation are required to accurately represent the measurements of particles that are dispersed in solution. 83 Readers interested in these methods are encouraged to read the recent perspective by Googasian *et al.* 82 With these considerations in mind, simulations based on electron tomography are becoming increasingly common. For example, the differential electric field enhancement around 4-fold twisted gold nanorods was visualized depending on the handedness of a circularly polarized illumination (**Figure 5c, d**). 18 The distribution of electric field enhancement at the surface of nanotriskelions with multiple 3-fold and 4-fold chiral centers could also be maped, showing differences in the excitation of the chiral centers as a function of the light polarization. 84

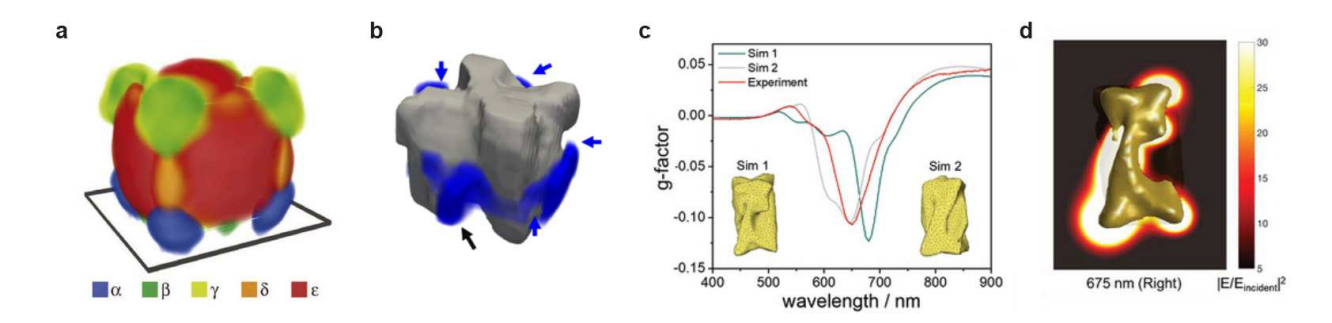


Figure 5: Probing chiroptical properties with 3D-EM. (a) 3D mapping of surface plasmon modes with multimode ET and EELS for an achiral Ag nanocube. Reproduced with permission from ref ²³. Copyright 2013, Springer Nature. (b) 3D mapping of a surface plasmon mode for a chiral gold helicoid. The blue band is the reconstruction of a spectral component corresponding to a chiral mode at 2.27 eV. Reproduced with permission from ref ²². Copyright 2024, American Chemical Society. (c) Conventional ET reconstruction used as the input for electromagnetic field simulations of *g*-factor spectra and compared to the experimental spectrum. (d) Distribution of the electric field enhancement under right-handed circularly polarized illumination at 675 nm. (c, d) Reproduced with permission from ref ¹⁸. Available under a CC-BY 4.0. Copyright 2022, The Authors.

4. 3D EM to understand chiral morphogenesis

Beyond understanding and optimizing chiral shapes for specific optical properties, it is important to advance the synthetic toolbox by gaining mechanistic insight into chiral morphogenesis. Understanding how chiral features emerge requires visualizing and, ideally, quantitatively monitoring the morphological evolution from achiral seed precursors to the final product. For this, 3D EM, in combination with adequate experimental design, has been shown to be excellently suited. For example, SEM was used to visualize the evolution of the 432 Au helicoids first developed by Nam and coworkers. ¹⁷ Growth series were first obtained by quenching the slow growth reaction at specific time intervals, and SEM images of the products at each step were subsequently acquired. The series revealed the gradual emergence of chiral edges and mirror plane removal from the initial stellated octahedron.¹⁷ For morphologies with finer features, the acceleration of electron tomography acquisition and reconstruction has been largely beneficial. In two relevant cases, the morphological transitions in wrinkled Au particles obtained using micelle-templated chiral growth could be revealed.^{2,25,26} In this approach, helical, worm-like micelles would coil around nanorod seeds with a defined pitch and template the growth of fine surface structures. To visualize this, growth series were first synthesized by running parallel reactions with varying concentration of reactants, and the resulting products could be isolated and reconstructed with tomography thereafter (Figure 6a). ²⁶ More recently, a kinetic series protocol was established in which growth in parallel reactions was halted at incremental time points by fast addition of NaBH₄, a strong reducing agent. Here again, tomographic reconstruction of the isolated products at each step allowed to visualize the morphological evolution of the products (Figure 6b).²⁵ In this instance,

both series consistently revealed that on single-crystalline seeds, a first intermediate with quasi-square cross section and 12 facets was produced before any wrinkles start to grow. Owing to the HAADF contrast, electron tomography is also adequate to differentiate between materials within reconstructions. This effect was for instance used to gain insights into the onset of gold wrinkle formation.²⁶ A Pd interlayer was deposited on Au seeds prior to wrinkle growth, and its position could be retrieved in the electron tomography reconstruction (**Figure 6c**). These results confirmed that an intermediate structure was required for wrinkle growth on single-crystalline seeds, but also that the influence of the structure and geometry of the seeds on the final wrinkled morphology warrants further investigation.

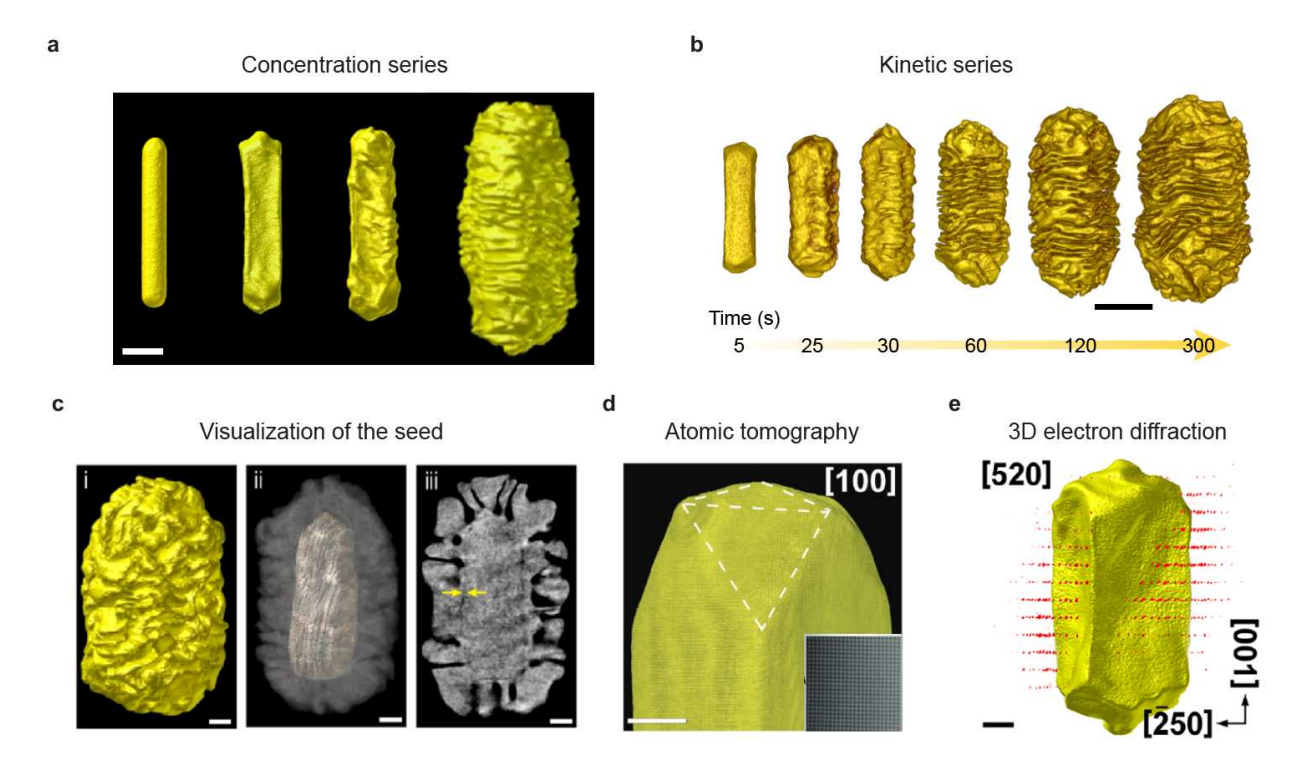


Figure 6: 3D EM to understand the growth mechanisms of chiral gold nanocrystals. (a) Conventional electron tomography yields morphological information that can be used to track the development of features across growth conditions and / or (b) time, here during the growth of gold helical wrinkles of single-crystalline gold NRs templated by helical micelles. (c) Visualization a Pd interlayer with electron tomography to understand the growth of chiral features on a gold nanorod seed. (d) Structural information can further be obtained with atomic-resolution electron tomography, here on a growth intermediate of twisted NRs after one chiral growth step in the presence of *L*-cysteine; or (c) by combining conventional tomography with 3D electron diffraction, here on a twisted gold NR. Scale bars are 20 nm (a), 50 nm (b), 10 nm (c, d) and 25 nm (e). (a, c) Adapted with permission from ref ²⁶. Copyright 2022, American Chemical Society. (b) Adapted with permission from ref ²⁵. Copyright 2025, American Chemical Society. (d) Adapted with permission from ref ²⁶. Available under a CC-BY 4.0. Copyright 2022, The Authors. (e) Reproduced with permission from ref ²⁴. Available under a CC-BY 4.0. Copyright 2023, The Authors.

The structure and facets of the products are furthermore crucial to understand and rationalize the growth pathway, but are often more challenging than the morphology to retrieve unambiguously. When products are sharply faceted, the surface structure can be obtained using a combination of high resolution (HR)TEM, electron diffraction and conventional electron tomography or SEM / SEEBIC images. 66 For example, the angles between the facets of the nanorod intermediate with quasi-square described above can only be obtained by {110} facets, while it could be concluded using SEM and HRTEM that the stellated octahedron seeds for helicoid growth are enclosed by {321} facets. ¹⁷ However, chiral particles are often complex and poorly facetted (rounded), and sometimes possess structural defects that challenge the interpretation of diffraction patterns and projection images.³⁰ To explicitly retrieve the 3D structure, atomic-resolution electron tomography (AET) is one of the most powerful techniques and has been largely applied to plasmonic nanostructures. 18,34,35,85,86 AET has for instance confirmed the surface structure of nanorod seeds used for chiral overgrowth, resolving that single-crystalline gold nanorods are enclosed by a combination of {100}, {110} and {520} facets.³⁵ During the growth of twisted gold nanorods in presence of cysteine as the chiral inducer, it was shown that an intermediate structure with {520} facets at the tips was first obtained (Figure 6d), which then allowed chiral {521} facets to be stabilized by the chiral additive. 18 However, AET requires particles to be relatively small, typically 20 nm at most for the reconstructions to be unambiguous, and is therefore limited to the characterization of the early stages of growth. For larger particles, it has recently been proposed to combine conventional ET reconstructions with 3D electron diffraction. For twisted gold nanorods, a 3D reconstruction of the reciprocal lattice was obtained and oriented in relation to the 3D reconstruction of the particle (Figure 6e). ²⁴ It was demonstrated that the chiral features were close to {520} facets, and therefore likely included {521} planes with atomic chirality.

5. Conclusions and Outlook

The qualitative and quantitative analysis of 3D EM data has demonstrated unparalleled advantages for the study of the complex morphologies and structure-property relations in chiral nanoparticles. Visualization of the nanometer-scale surface topography using SEM and SEEBIC and explicit retrieval of 3D volumes with electron tomography allow us to unambiguously determine the handedness of helical shapes and relate it to their chiroptical properties. Quantitative chirality measures can contribute to explaining the origin of chiroptical signals and may support their optimization. In combination with dedicated experimental planning, the systematic investigation of synthesis products with 3D EM helps reveal growth pathways, while structural investigations grant mechanistic insights towards the rational synthesis of chiral products.

This Mini Review shows that 3D characterization is already essential to the development of chiral nanoparticles with targeted shapes and properties, and further advancements will continue to offer new opportunities and insights. We propose, as conclusion and outlook, a few exciting avenues towards such improved microscopies. While these are described within the context of guiding the synthesis of novel and optimized chiral nanomaterials, they will undoubdetdly benefit the many other nanosystems where statistical insights, throughput and a relevant environment are important.

- 1. Higher information throughput. Increasing the information throughput of 3D EM is crucial to account for the statistical diversity in chiral synthesis and truly systematize 3D characterization. At present, 3D EM can either provide detailed information on a few particles with electron tomography, or limited data on many particles using SEM and SEEBIC. Although it appears difficult to accelerate electron tomography acquisition beyond the few tens of particles per day that can be investigated at present (in ideal cases), greater automation of the acquisition and reconstruction procedure, as observed in structural biology, could free the operator and allow them to focus on data interpretation. On the other hand, the design of novel shape descriptors operating on surface images would afford novel information to be extracted from SEM and SEEBIC images. The use of SEM photogrammetry for chiral products remains an underexplored area towards faster 3D characterization, and assessing the resolution limits of the established methods would be important. SEEBIC too could lend itself to 3D retrieval, if a "shadowing" mechanism can be implemented, e.g., through the integration of multiple electrodes in the specimen holder. Alternatively, it appears that the combination of a surface and a transmission image, as simultaneously acquired in SEEBIC and HAADF-STEM, would contain rich 3D information about the imaged sample. Even though no volumetric reconstruction method can currently use both images at the same time, there is promise that solving this inverse problem will lead to a novel method for 3D retrieval with high throughput and high resolution.
- 2. Improved statistical data treatment. With increasing information, the use of statistical learning tools will also become important. Statistical models and dimensionality reduction methods could help reveal complex associations between shape and optical descriptors. Furthermore, combination of designed chiral measures and shape descriptors could be retrieved, offering better explanation of the optical properties. Such unified descriptors have already shown promise to predict the interaction of chiral particles with biomolecules.⁶⁷
- 3. 3D EM in aqueous environment and ligand imaging. For a comprehensive understanding of growth mechanisms, key insights about the structure and behavior of chirality inducers in the native synthesis environment are still lacking. At present, the ligands are typically removed to prevent contamination, and the contrast mechanism of STEM-HAADF tomography challenges their visualization in the first place. They are however central in the process of chirality emergence, ¹² and visualizing their spatial configuration could for example improve the understanding micelle-templating, or that of the surface-specific adsorption of

shape-directing amino acids. Cryo-ET, in combination with phase imaging such as ptychographic tomography could eventually resolve the ligands and possibly their hydrated conformation around the seeds.⁸⁷⁻⁹⁰ As an alternative, liquid-phase (LP)TEM using either graphene encapsulation or assembled microcells has already shown promises as shape-directing ligands have been visualized in 2D.⁹¹ Finally, the contrast of organic materials in SEEBIC warrants further investigations and could also offer a new way to visualize soft-hard interfaces.

4. Monitoring growth in real time and in 3D. As the effect of e-beam interactions with water becomes better understood, the beam could be integrated as a reducing agent to visualize the growth of particles, possibly in 3D and in real time. 92,93 Alternatively, mixing holders would allow for more faithful growth conditions. This goal will require the development of dynamic 3D EM, for instance via the integration of SEEBIC on *in situ* specimen holders or novel algorithms for dynamic ET.

ACKNOWLEDGEMENTS. The authors acknowledge financial support by the European Research Council (ERC SyG No. 101166855 CHIRAL-PRO to L.L.M and S.B.) and by the EU through the HORIZON EUROPE MSCA SE project DELIGHT (101131111). R.G. acknowledges the support of a FWO fellowship under award 12A1V25N.

REFERENCES

- (1) Carter, C. B.; Williams, D. B. Transmission Electron Microscopy; Springer US, 2016.
- (2) González-Rubio, G.; Mosquera, J.; Kumar, V.; Pedrazo-Tardajos, A.; Llombart, P.; Solís, D. M.; Lobato, I.; Noya, E. G.; Guerrero-Martínez, A.; Taboada, J. M.; Obelleiro, F.; MacDowell, L. G.; Bals, S.; Liz-Marzán, L. M. Micelle-Directed Chiral Seeded Growth on Anisotropic Gold Nanocrystals. *Science* **2020**, *368* (6498), 1472–1477. https://doi.org/10.1126/science.aba0980.
- (3) Li, Y.; Lin, H.; Zhou, W.; Sun, L.; Samanta, D.; Mirkin, C. A. Corner-, Edge-, and Facet-Controlled Growth of Nanocrystals. *Science Advances* **2021**, 7 (3), eabf1410. https://doi.org/10.1126/sciadv.abf1410.
- (4) Midgley, P. A.; Weyland, M. 3D Electron Microscopy in the Physical Sciences: The Development of Z-Contrast and EFTEM Tomography. *Ultramicroscopy* **2003**, *96* (3), 413–431. https://doi.org/10.1016/S0304-3991(03)00105-0.
- (5) Jenkinson, K.; Liz-Marzán, L. M.; Bals, S. Multimode Electron Tomography Sheds Light on Synthesis, Structure, and Properties of Complex Metal-Based Nanoparticles. *Adv. Mater.* **2022**, *34* (36), 2110394. https://doi.org/10.1002/adma.202110394.
- (6) Albrecht, W.; Bals, S. Fast Electron Tomography for Nanomaterials. *J. Phys. Chem. C* **2020**, *124* (50), 27276–27286. https://doi.org/10.1021/acs.jpcc.0c08939.
- (7) Hawkes, P. W.; Spence, J. C. H. *Springer Handbook of Microscopy*; Springer Handbooks; Springer International Publishing: Cham, 2019. https://doi.org/10.1007/978-3-030-00069-1.
- (8) Midgley, P. A.; Dunin-Borkowski, R. E. Electron Tomography and Holography in Materials Science. *Nature Mater* **2009**, *8* (4), 271–280. https://doi.org/10.1038/nmat2406.
- (9) Vlasov, E.; Skorikov, A.; Sánchez-Iglesias, A.; Liz-Marzán, L. M.; Verbeeck, J.; Bals, S. Secondary Electron Induced Current in Scanning Transmission Electron Microscopy: An Alternative Way to

- Visualize the Morphology of Nanoparticles. *ACS Materials Lett.* **2023**, *5* (7), 1916–1921. https://doi.org/10.1021/acsmaterialslett.3c00323.
- (10) Vlasov, E.; Heyvaert, W.; Ni, B.; Van Gordon, K.; Girod, R.; Verbeeck, J.; Liz-Marzán, L. M.; Bals, S. High-Throughput Morphological Chirality Quantification of Twisted and Wrinkled Gold Nanorods. *ACS Nano* **2024**, *18* (18), 12010–12019. https://doi.org/10.1021/acsnano.4c02757.
- (11) Chen, J.; Chen, X.; Murakami, R.-I.; Li, H.; Yu, X.; Feng, W.; Yang, Y.; Wang, P.; Zheng, G.; Tang, Z.; Wu, X. Chiral Inorganic Nanomaterials Characterized by Advanced TEM: A Qualitative and Quantitative Study. *Adv. Mater.* **2024**, *36* (49), 2410676. https://doi.org/10.1002/adma.202410676.
- (12)Ni, B.; González-Rubio, G.; Van Gordon, K.; Bals, S.; Kotov, N. A.; Liz-Marzán, L. M. Seed-Mediated Growth and Advanced Characterization of Chiral Gold Nanorods. *Adv. Mater.* **2024**, *36* (47), 2412473. https://doi.org/10.1002/adma.202412473.
- (13)Zheng, G.; He, J.; Kumar, V.; Wang, S.; Pastoriza-Santos, I.; Pérez-Juste, J.; Liz-Marzán, L. M.; Wong, K.-Y. Discrete Metal Nanoparticles with Plasmonic Chirality. *Chem. Soc. Rev.* **2021**, *50* (6), 3738–3754. https://doi.org/10.1039/C9CS00765B.
- (14) Kotov, N. A.; Liz-Marzán, L. M.; Weiss, P. S. Chiral Nanostructures: New Twists. *ACS Nano* **2021**, *15* (8), 12457–12460. https://doi.org/10.1021/acsnano.1c06959.
- (15)Kim, J.-Y.; Yeom, J.; Zhao, G.; Calcaterra, H.; Munn, J.; Zhang, P.; Kotov, N. Assembly of Gold Nanoparticles into Chiral Superstructures Driven by Circularly Polarized Light. *J. Am. Chem. Soc.* **2019**, *141* (30), 11739–11744. https://doi.org/10.1021/jacs.9b00700.
- (16)Xu, L.; Wang, X.; Wang, W.; Sun, M.; Choi, W. J.; Kim, J.-Y.; Hao, C.; Li, S.; Qu, A.; Lu, M.; Wu, X.; Colombari, F. M.; Gomes, W. R.; Blanco, A. L.; de Moura, A. F.; Guo, X.; Kuang, H.; Kotov, N. A.; Xu, C. Enantiomer-Dependent Immunological Response to Chiral Nanoparticles. *Nature* **2022**, *601* (7893), 366–373. https://doi.org/10.1038/s41586-021-04243-2.
- (17)Lee, H.-E.; Ahn, H.-Y.; Mun, J.; Lee, Y. Y.; Kim, M.; Cho, N. H.; Chang, K.; Kim, W. S.; Rho, J.; Nam, K. T. Amino-Acid- and Peptide-Directed Synthesis of Chiral Plasmonic Gold Nanoparticles. *Nature* **2018**, *556* (7701), 360–365. https://doi.org/10.1038/s41586-018-0034-1.
- (18)Ni, B.; Mychinko, M.; Gómez-Graña, S.; Morales-Vidal, J.; Obelleiro-Liz, M.; Heyvaert, W.; Vila-Liarte, D.; Zhuo, X.; Albrecht, W.; Zheng, G.; González-Rubio, G.; Taboada, J. M.; Obelleiro, F.; López, N.; Pérez-Juste, J.; Pastoriza-Santos, I.; Cölfen, H.; Bals, S.; Liz-Marzán, L. M. Chiral Seeded Growth of Gold Nanorods Into Fourfold Twisted Nanoparticles with Plasmonic Optical Activity. *Adv. Mater.* 2023, *35* (1), 2208299. https://doi.org/10.1002/adma.202208299.
- (19) Kumar, P.; Vo, T.; Cha, M.; Visheratina, A.; Kim, J.-Y.; Xu, W.; Schwartz, J.; Simon, A.; Katz, D.; Nicu, V. P.; Marino, E.; Choi, W. J.; Veksler, M.; Chen, S.; Murray, C.; Hovden, R.; Glotzer, S.; Kotov, N. A. Photonically Active Bowtie Nanoassemblies with Chirality Continuum. *Nature* **2023**, *615* (7952), 418–424. https://doi.org/10.1038/s41586-023-05733-1.
- (20) Choi, W. J.; Lee, S. H.; Cha, M.; Kotov, N. A. Chiral Kirigami for Bend-Tolerant Reconfigurable Hologram with Continuously Variable Chirality Measures. *Adv. Mater.* **2024**, *36* (30), 2401131. https://doi.org/10.1002/adma.202401131.
- (21) Heyvaert, W.; Pedrazo-Tardajos, A.; Kadu, A.; Claes, N.; González-Rubio, G.; Liz-Marzán, L. M.; Albrecht, W.; Bals, S. Quantification of the Helical Morphology of Chiral Gold Nanorods. *ACS Materials Lett.* **2022**, *4* (4), 642–649. https://doi.org/10.1021/acsmaterialslett.2c00055.
- (22) Jo, J.; Ryu, J.; Huh, J.-H.; Kim, H.; Seo, D. H.; Lee, J.; Kwon, M.; Lee, S.; Nam, K. T.; Kim, M. Direct Three-Dimensional Observation of the Plasmonic Near-Fields of a Nanoparticle with Circular Dichroism. *ACS Nano* **2024**. https://doi.org/10.1021/acsnano.4c10677.
- (23) Nicoletti, O.; de la Peña, F.; Leary, R. K.; Holland, D. J.; Ducati, C.; Midgley, P. A. Three-Dimensional Imaging of Localized Surface Plasmon Resonances of Metal Nanoparticles. *Nature* **2013**, *502* (7469), 80–84. https://doi.org/10.1038/nature12469.
- (24) Van Gordon, K.; Baúlde, S.; Mychinko, M.; Heyvaert, W.; Obelleiro-Liz, M.; Criado, A.; Bals, S.; Liz-Marzán, L. M.; Mosquera, J. Tuning the Growth of Chiral Gold Nanoparticles Through Rational Design of a Chiral Molecular Inducer. *Nano Lett.* **2023**, *23* (21), 9880–9886. https://doi.org/10.1021/acs.nanolett.3c02800.

- (25) Van Gordon, K.; Girod, R.; Bevilacqua, F.; Bals, S.; Liz-Marzán, L. M. Structural and Optical Characterization of Reaction Intermediates during Fast Chiral Nanoparticle Growth. *Nano Lett.* **2025**, 25 (7), 2887–2893. https://doi.org/10.1021/acs.nanolett.4c06145.
- (26)Zhuo, X.; Mychinko, M.; Heyvaert, W.; Larios, D.; Obelleiro-Liz, M.; Taboada, J. M.; Bals, S.; Liz-Marzán, L. M. Morphological and Optical Transitions during Micelle-Seeded Chiral Growth on Gold Nanorods. *ACS Nano* **2022**, *16* (11), 19281–19292. https://doi.org/10.1021/acsnano.2c08668.
- (27) Erdman, N.; Bell, D. C.; Reichelt, R. Scanning Electron Microscopy. In *Springer Handbook of Microscopy*; Hawkes, P. W., Spence, J. C. H., Eds.; Springer Handbooks; Springer International Publishing: Cham, 2019; pp 229–318. https://doi.org/10.1007/978-3-030-00069-1 5.
- (28) Tafti, A. P.; Kirkpatrick, A. B.; Alavi, Z.; Owen, H. A.; Yu, Z. Recent Advances in 3D SEM Surface Reconstruction. *Micron* **2015**, *78*, 54–66. https://doi.org/10.1016/j.micron.2015.07.005.
- (29) Gontard, L. C.; López-Castro, J. D.; González-Rovira, L.; Vázquez-Martínez, J. M.; Varela-Feria, F. M.; Marcos, M.; Calvino, J. J. Assessment of Engineered Surfaces Roughness by High-Resolution 3D SEM Photogrammetry. *Ultramicroscopy* **2017**, *177*, 106–114. https://doi.org/10.1016/j.ultramic.2017.03.007.
- (30) Van Gordon, K.; Ni, B.; Girod, R.; Mychinko, M.; Bevilacqua, F.; Bals, S.; Liz-Marzán, L. M. Single Crystal and Pentatwinned Gold Nanorods Result in Chiral Nanocrystals with Reverse Handedness. *Angew. Chem. Int. Ed.* **2024**, *63* (26), e202403116. https://doi.org/10.1002/anie.202403116.
- (31) Vanrompay, H.; Skorikov, A.; Bladt, E.; Béché, A.; Freitag, B.; Verbeeck, J.; Bals, S. Fast versus Conventional HAADF-STEM Tomography of Nanoparticles: Advantages and Challenges. *Ultramicroscopy* **2021**, *221*, 113191. https://doi.org/10.1016/j.ultramic.2020.113191.
- (32) Vanrompay, H.; Bladt, E.; Albrecht, W.; Béché, A.; Zakhozheva, M.; Sánchez-Iglesias, A.; M. Liz-Marzán, L.; Bals, S. 3D Characterization of Heat-Induced Morphological Changes of Au Nanostars by Fast in Situ Electron Tomography. *Nanoscale* **2018**, *10* (48), 22792–22801. https://doi.org/10.1039/C8NR08376B.
- (33) Altantzis, T.; Wang, D.; Kadu, A.; van Blaaderen, A.; Bals, S. Optimized 3D Reconstruction of Large, Compact Assemblies of Metallic Nanoparticles. *J. Phys. Chem. C* **2021**, *125* (47), 26240–26246. https://doi.org/10.1021/acs.jpcc.1c08478.
- (34) Albrecht, W.; Arslan Irmak, E.; Altantzis, T.; Pedrazo-Tardajos, A.; Skorikov, A.; Deng, T.-S.; van der Hoeven, J. E. S.; van Blaaderen, A.; Van Aert, S.; Bals, S. 3D Atomic-Scale Dynamics of Laser-Light-Induced Restructuring of Nanoparticles Unraveled by Electron Tomography. *Adv. Mater.* **2021**, *33* (33), 2100972. https://doi.org/10.1002/adma.202100972.
- (35) Goris, B.; Bals, S.; Van den Broek, W.; Carbó-Argibay, E.; Gómez-Graña, S.; Liz-Marzán, L. M.; Van Tendeloo, G. Atomic-Scale Determination of Surface Facets in Gold Nanorods. *Nat. Mater.* **2012**, *11* (11), 930–935. https://doi.org/10.1038/nmat3462.
- (36) Neggers, J.; Héripré, E.; Bonnet, M.; Boivin, D.; Tanguy, A.; Hallais, S.; Gaslain, F.; Rouesne, E.; Roux, S. Principal Image Decomposition for Multi-Detector Backscatter Electron Topography Reconstruction. *Ultramicroscopy* **2021**, *227*, 113200. https://doi.org/10.1016/j.ultramic.2020.113200.
- (37) Kozikowski, P. Extracting Three-Dimensional Information from SEM Images by Means of Photogrammetry. *Micron* **2020**, *134*, 102873. https://doi.org/10.1016/j.micron.2020.102873.
- (38) Spaeth, P.; Adhikari, S.; Heyvaert, W.; Zhuo, X.; García, I.; Liz-Marzán, L. M.; Bals, S.; Orrit, M.; Albrecht, W. Photothermal Circular Dichroism Measurements of Single Chiral Gold Nanoparticles Correlated with Electron Tomography. *ACS Photonics* **2022**, *9* (12), 3995–4004. https://doi.org/10.1021/acsphotonics.2c01457.
- (39) Hugenschmidt, M.; Jannis, D.; Kadu, A. A.; Grünewald, L.; De Marchi, S.; Pérez-Juste, J.; Verbeeck, J.; Van Aert, S.; Bals, S. Low-Dose 4D-STEM Tomography for Beam-Sensitive Nanocomposites. *ACS Materials Lett.* **2024**, *6* (1), 165–173. https://doi.org/10.1021/acsmaterialslett.3c01042.
- (40) Albrecht, W.; Bladt, E.; Vanrompay, H.; Smith, J. D.; Skrabalak, S. E.; Bals, S. Thermal Stability of Gold/Palladium Octopods Studied *in Situ* in 3D: Understanding Design Rules for Thermally Stable Metal Nanoparticles. *ACS Nano* **2019**, *13* (6), 6522–6530. https://doi.org/10.1021/acsnano.9b00108.

- (41) Williams, D. B.; Carter, C. B. *Transmission Electron Microscopy: A Textbook for Materials Science*, 2nd ed.; Springer: New York, 2008.
- (42) Weyland, M.; Midgley, P. A.; Thomas, J. M. Electron Tomography of Nanoparticle Catalysts on Porous Supports: A New Technique Based on Rutherford Scattering. *J. Phys. Chem. B* **2001**, *105* (33), 7882–7886. https://doi.org/10.1021/jp011566s.
- (43)Leary, R.; Saghi, Z.; Midgley, P. A.; Holland, D. J. Compressed Sensing Electron Tomography. *Ultramicroscopy* **2013**, *131*, 70–91. https://doi.org/10.1016/j.ultramic.2013.03.019.
- (44) Goris, B.; Van den Broek, W.; Batenburg, K. J.; Heidari Mezerji, H.; Bals, S. Electron Tomography Based on a Total Variation Minimization Reconstruction Technique. *Ultramicroscopy* **2012**, *113*, 120–130. https://doi.org/10.1016/j.ultramic.2011.11.004.
- (45)Zanaga, D.; Bleichrodt, F.; Altantzis, T.; Winckelmans, N.; Palenstijn, W. J.; Sijbers, J.; De Nijs, B.; Van Huis, M. A.; Sánchez-Iglesias, A.; Liz-Marzán, L. M.; Van Blaaderen, A.; Joost Batenburg, K.; Bals, S.; Van Tendeloo, G. Quantitative 3D Analysis of Huge Nanoparticle Assemblies. *Nanoscale* **2016**, 8 (1), 292–299. https://doi.org/10.1039/C5NR06962A.
- (46)Ren, D.; Ophus, C.; Chen, M.; Waller, L. A Multiple Scattering Algorithm for Three Dimensional Phase Contrast Atomic Electron Tomography. *Ultramicroscopy* **2020**, *208*, 112860. https://doi.org/10.1016/j.ultramic.2019.112860.
- (47) Venkatakrishnan, S. V.; Drummy, L. F.; Jackson, M. A.; De Graef, M.; Simmons, J.; Bouman, C. A. A Model Based Iterative Reconstruction Algorithm For High Angle Annular Dark Field-Scanning Transmission Electron Microscope (HAADF-STEM) Tomography. *IEEE Trans. Image Processing* **2013**, *22* (11), 4532–4544. https://doi.org/10.1109/TIP.2013.2277784.
- (48) Scott, M. C.; Chen, C.-C.; Mecklenburg, M.; Zhu, C.; Xu, R.; Ercius, P.; Dahmen, U.; Regan, B. C.; Miao, J. Electron Tomography at 2.4-Ångström Resolution. *Nature* **2012**, *483* (7390), 444–447. https://doi.org/10.1038/nature10934.
- (49)Zhong, Z.; Goris, B.; Schoenmakers, R.; Bals, S.; Batenburg, K. J. A Bimodal Tomographic Reconstruction Technique Combining EDS-STEM and HAADF-STEM. *Ultramicroscopy* **2017**, *174*, 35–45. https://doi.org/10.1016/j.ultramic.2016.12.008.
- (50) Schwartz, J.; Di, Z. W.; Jiang, Y.; Manassa, J.; Pietryga, J.; Qian, Y.; Cho, M. G.; Rowell, J. L.; Zheng, H.; Robinson, R. D.; Gu, J.; Kirilin, A.; Rozeveld, S.; Ercius, P.; Fessler, J. A.; Xu, T.; Scott, M.; Hovden, R. Imaging 3D Chemistry at 1 Nm Resolution with Fused Multi-Modal Electron Tomography. *Nat. Commun.* **2024**, *15* (1), 3555. https://doi.org/10.1038/s41467-024-47558-0.
- (51)Sa, J.; Hu, N.; Heyvaert, W.; Van Gordon, K.; Li, H.; Wang, L.; Bals, S.; Liz-Marzán, L. M.; Ni, W. Spontaneous Chirality Evolved at the Au–Ag Interface in Plasmonic Nanorods. *Chem. Mater.* **2023**, *35* (17), 6782–6789. https://doi.org/10.1021/acs.chemmater.3c01044.
- (52) Eggeman, A. S.; Krakow, R.; Midgley, P. A. Scanning Precession Electron Tomography for Three-Dimensional Nanoscale Orientation Imaging and Crystallographic Analysis. *Nat. Commun.* **2015**, *6* (1), 7267. https://doi.org/10.1038/ncomms8267.
- (53) Leary, R. K.; Midgley, P. A. Electron Tomography in Materials Science. In *Springer Handbook of Microscopy*; Hawkes, P. W., Spence, J. C. H., Eds.; Springer International Publishing: Cham, 2019.
- (54)Roiban, L.; Li, S.; Aouine, M.; Tuel, A.; Farrusseng, D.; Epicier, T. Fast 'Operando' Electron Nanotomography. *Journal of Microscopy* **2018**, *269* (2), 117–126. https://doi.org/10.1111/jmi.12557.
- (55) Albrecht, W.; Van Aert, S.; Bals, S. Three-Dimensional Nanoparticle Transformations Captured by an Electron Microscope. *Acc. Chem. Res.* **2021**, *54* (5), 1189–1199. https://doi.org/10.1021/acs.accounts.0c00711.
- (56) Arenas Esteban, D.; Wang, D.; Kadu, A.; Olluyn, N.; Sánchez-Iglesias, A.; Gomez-Perez, A.; González-Casablanca, J.; Nicolopoulos, S.; Liz-Marzán, L. M.; Bals, S. Quantitative 3D Structural Analysis of Small Colloidal Assemblies under Native Conditions by Liquid-Cell Fast Electron Tomography. *Nat. Commun.* **2024**, *15* (1), 6399. https://doi.org/10.1038/s41467-024-50652-y.
- (57) Egerton, R. F. Radiation Damage to Organic and Inorganic Specimens in the TEM. *Micron* **2019**, *119*, 72–87. https://doi.org/10.1016/j.micron.2019.01.005.

- (58) *Electron Tomography: Methods for Three-Dimensional Visualization of Structures in the Cell*, 2nd ed.; Frank, J., Ed.; Springer: New York; London, 2006.
- (59)Inada, H.; Zhu, Y. Secondary Electron Microscopy in STEM. In *Scanning Transmission Electron Microscopy of Nanomaterials*; Imperial College Press, 2014; pp 307–344. https://doi.org/10.1142/9781848167902 0010.
- (60) Mecklenburg, M.; Hubbard, W. A.; Lodico, J. J.; Regan, B. C. Electron Beam-Induced Current Imaging with Two-Angstrom Resolution. *Ultramicroscopy* **2019**, 207, 112852. https://doi.org/10.1016/j.ultramic.2019.112852.
- (61) Sun, X.; Yang, J.; Sun, L.; Yang, G.; Liu, C.; Tao, Y.; Cheng, Q.; Wang, C.; Xu, H.; Zhang, Q. Tunable Reversal of Circular Dichroism in the Seed-Mediated Growth of Bichiral Plasmonic Nanoparticles. *ACS Nano* **2022**, *16* (11), 19174–19186. https://doi.org/10.1021/acsnano.2c08381.
- (62)Petitjean, M. Chirality and Symmetry Measures: A Transdisciplinary Review. *Entropy* **2003**, *5* (3), 271–312. https://doi.org/10.3390/e5030271.
- (63)Buda, A. B.; Mislow, K. A Hausdorff Chirality Measure. *J. Am. Chem. Soc.* **1992**, *114* (15), 6006–6012. https://doi.org/10.1021/ja00041a016.
- (64) Yao, L.-Y.; Qin, L.; Chen, Z.; Lam, J.; Yam, V. W.-W. Assembly of Luminescent Chiral Gold(I)-Sulfido Clusters via Chiral Self-Sorting. *Angew. Chem. Int. Ed.* **2023**, *63* (6), e202316200. https://doi.org/10.1002/anie.202316200.
- (65) Girod, R.; Mychinko, M.; Van Gordon, K.; Ni, B.; Bevilacqua, F.; Liz-Marzan, L.; Bals, S. Quantification of Chirality from Electron Tomography Data. *BIO Web Conf.* **2024**, *129*, 02009. https://doi.org/10.1051/bioconf/202412902009.
- (66)Bevilacqua, F.; Girod, R.; Martín, V. F.; Obelleiro-Liz, M.; Vinnacombe-Willson, G. A.; Van Gordon, K.; Hofkens, J.; Taboada, J. M.; Bals, S.; Liz-Marzán, L. M. Additive-Free Synthesis of (Chiral) Gold Bipyramids from Pentatwinned Nanorods. *ACS Materials Lett.* **2024**, *6* (11), 5163–5169. https://doi.org/10.1021/acsmaterialslett.4c01605.
- (67) Cha, M.; Emre, E. S. T.; Xiao, X.; Kim, J.-Y.; Bogdan, P.; VanEpps, J. S.; Violi, A.; Kotov, N. A. Unifying Structural Descriptors for Biological and Bioinspired Nanoscale Complexes. *Nat. Comput. Sci.* **2022**, *2* (4), 243–252. https://doi.org/10.1038/s43588-022-00229-w.
- (68) Cha, M.; Ma, J.; Kim, J.-Y.; Emre, E. S. T.; Kotov, N. A. Graph-Theoretical Chirality Measure and Chirality—Property Relations for Chemical Structures with Multiscale Mirror Asymmetries. *Chirality* **2024**, *36* (6), e23678. https://doi.org/10.1002/chir.23678.
- (69)Osipov, M. A.; Pickup, B. T.; Dunmur, D. A. A New Twist to Molecular Chirality: Intrinsic Chirality Indices. *Mol. Phys.* **1995**, *84* (6), 1193–1206. https://doi.org/10.1080/00268979500100831.
- (70)Millar, G.; Weinberg, N.; Mislow, K. On the Osipov–Pickup–Dunmur Chirality Index: Why Pseudoscalar Functions Are Generally Unsuitable to Quantify Chirality. *Mol. Phys.* **2005**, *103* (20), 2769–2772. https://doi.org/10.1080/00268970500217196.
- (71)Ben-Moshe, A.; Da Silva, A.; Müller, A.; Abu-Odeh, A.; Harrison, P.; Waelder, J.; Niroui, F.; Ophus, C.; Minor, A. M.; Asta, M.; Theis, W.; Ercius, P.; Alivisatos, A. P. The Chain of Chirality Transfer in Tellurium Nanocrystals. *Science* **2021**, *372* (6543), 729–733. https://doi.org/10.1126/science.abf9645.
- (72) Visheratina, A.; Visheratin, A.; Kumar, P.; Veksler, M.; Kotov, N. A. Chirality Analysis of Complex Microparticles Using Deep Learning on Realistic Sets of Microscopy Images. *ACS Nano* **2023**, *17* (8), 7431–7442. https://doi.org/10.1021/acsnano.2c12056.
- (73) Groschner, C. K.; Pattison, A. J.; Ben-Moshe, A.; Alivisatos, A. P.; Theis, W.; Scott, M. C. Classifying Handedness in Chiral Nanomaterials Using Label Error Robust Deep Learning. *npj Comput. Mater.* **2022**, *8* (1), 149. https://doi.org/10.1038/s41524-022-00822-7.
- (74) Fowler, P. W. Quantification of Chirality: Attempting the Impossible. *Symmetry: Culture and Science* **2005**, *16* (4), 321–334.
- (75)Petitjean, M. Chirality in Metric Spaces: In Memoriam Michel Deza. *Optim. Lett.* **2020**, *14* (2), 329–338. https://doi.org/10.1007/s11590-017-1189-7.

- (76) Archanjo, B. S.; Vasconcelos, T. L.; Oliveira, B. S.; Song, C.; Allen, F. I.; Achete, C. A.; Ercius, P. Plasmon 3D Electron Tomography and Local Electric-Field Enhancement of Engineered Plasmonic Nanoantennas. *ACS Photonics* **2018**, *5* (7), 2834–2842. https://doi.org/10.1021/acsphotonics.8b00125.
- (77) Haberfehlner, G.; Schmidt, F.-P.; Schaffernak, G.; Hörl, A.; Trügler, A.; Hohenau, A.; Hofer, F.; Krenn, J. R.; Hohenester, U.; Kothleitner, G. 3D Imaging of Gap Plasmons in Vertically Coupled Nanoparticles by EELS Tomography. *Nano Lett.* **2017**, *17* (11), 6773–6777. https://doi.org/10.1021/acs.nanolett.7b02979.
- (78) Hörl, A.; Haberfehlner, G.; Trügler, A.; Schmidt, F.-P.; Hohenester, U.; Kothleitner, G. Tomographic Imaging of the Photonic Environment of Plasmonic Nanoparticles. *Nat. Commun.* **2017**, *8* (1), 37. https://doi.org/10.1038/s41467-017-00051-3.
- (79) Collins, S. M.; Ringe, E.; Duchamp, M.; Saghi, Z.; Dunin-Borkowski, R. E.; Midgley, P. A. Eigenmode Tomography of Surface Charge Oscillations of Plasmonic Nanoparticles by Electron Energy Loss Spectroscopy. *ACS Photonics* **2015**, *2* (11), 1628–1635. https://doi.org/10.1021/acsphotonics.5b00421.
- (80)Hörl, A.; Trügler, A.; Hohenester, U. Tomography of Particle Plasmon Fields from Electron Energy Loss Spectroscopy. *Phys. Rev. Lett.* **2013**, *111* (7), 076801. https://doi.org/10.1103/PhysRevLett.111.076801.
- (81) Dieperink, M.; Skorikov, A.; Claes, N.; Bals, S.; Albrecht, W. Considerations for Electromagnetic Simulations for a Quantitative Correlation of Optical Spectroscopy and Electron Tomography of Plasmonic Nanoparticles. *Nanophotonics* **2024**, *13* (25), 4647–4665. https://doi.org/10.1515/nanoph-2024-0238.
- (82) Googasian, J. S.; Skrabalak, S. E. Practical Considerations for Simulating the Plasmonic Properties of Metal Nanoparticles. *ACS Phys. Chem Au* **2023**, *3* (3), 252–262. https://doi.org/10.1021/acsphyschemau.2c00064.
- (83) Googasian, J. S.; Lewis, G. R.; Woessner, Z. J.; Ringe, E.; Skrabalak, S. E. Seed-Directed Synthesis of Chiroptically Active Au Nanocrystals of Varied Symmetries. *Chem. Commun.* **2022**, *58* (82), 11575–11578. https://doi.org/10.1039/D2CC04126J.
- (84) Zheng, J.; Boukouvala, C.; Lewis, G. R.; Ma, Y.; Chen, Y.; Ringe, E.; Shao, L.; Huang, Z.; Wang, J. Halide-Assisted Differential Growth of Chiral Nanoparticles with Threefold Rotational Symmetry. *Nat. Commun.* **2023**, *14* (1), 3783. https://doi.org/10.1038/s41467-023-39456-8.
- (85) Milagres de Oliveira, T.; Albrecht, W.; González-Rubio, G.; Altantzis, T.; Lobato Hoyos, I. P.; Béché, A.; Van Aert, S.; Guerrero-Martínez, A.; Liz-Marzán, L. M.; Bals, S. 3D Characterization and Plasmon Mapping of Gold Nanorods Welded by Femtosecond Laser Irradiation. *ACS Nano* **2020**, *14* (10), 12558–12570. https://doi.org/10.1021/acsnano.0c02610.
- (86) Goris, B.; De Beenhouwer, J.; De Backer, A.; Zanaga, D.; Batenburg, K. J.; Sánchez-Iglesias, A.; Liz-Marzán, L. M.; Van Aert, S.; Bals, S.; Sijbers, J.; Van Tendeloo, G. Measuring Lattice Strain in Three Dimensions through Electron Microscopy. *Nano Lett.* **2015**, *15* (10), 6996–7001. https://doi.org/10.1021/acs.nanolett.5b03008.
- (87)Hao, W.; Chesnokov, Y. M.; Molchanov, V. S.; Podlesnyi, P. R.; Kuklin, A. I.; Skoi, V. V.; Philippova, O. E. Cryo-Electron Tomography Study of the Evolution of Wormlike Micelles to Saturated Networks and Perforated Vesicles. *J. Coll. Interface Sci.* **2024**, *672*, 431–445. https://doi.org/10.1016/j.jcis.2024.06.011.
- (88)Ito, T. H.; Salles, A. G.; Priebe, J. P.; Miranda, P. C. M. L.; Morgon, N. H.; Danino, D.; Mancini, G.; Sabadini, E. Generation of a Chiral Giant Micelle. *Langmuir* **2016**, *32* (33), 8461–8466. https://doi.org/10.1021/acs.langmuir.6b02367.
- (89) Pelz, P. M.; Griffin, S. M.; Stonemeyer, S.; Popple, D.; DeVyldere, H.; Ercius, P.; Zettl, A.; Scott, M. C.; Ophus, C. Solving Complex Nanostructures with Ptychographic Atomic Electron Tomography. *Nat Commun* **2023**, *14* (1), 7906. https://doi.org/10.1038/s41467-023-43634-z.
- (90) Romanov, A.; Cho, M. G.; Scott, M. C.; Pelz, P. Multi-Slice Electron Ptychographic Tomography for Three-Dimensional Phase-Contrast Microscopy beyond the Depth of Focus Limits. *J. Phys. Mater.* **2025**, *8* (1), 015005. https://doi.org/10.1088/2515-7639/ad9ad2.

- (91) Pedrazo-Tardajos, A.; Claes, N.; Wang, D.; Sánchez-Iglesias, A.; Nandi, P.; Jenkinson, K.; De Meyer, R.; Liz-Marzán, L. M.; Bals, S. Direct Visualization of Ligands on Gold Nanoparticles in a Liquid Environment. *Nat. Chem.* **2024**, *16* (8), 1278–1285. https://doi.org/10.1038/s41557-024-01574-1.
- (92)Kim, J.; Kang, S.; Cheng, F.; Wang, Y.; Ye, X.; Park, J. Recent Advances in Liquid Phase Transmission Electron Microscopy of Nanoparticle Growth and Self-Assembly. *MRS Bull.* **2024**, *49* (4), 365–376. https://doi.org/10.1557/s43577-024-00702-z.
- (93) Woehl, T. J.; Moser, T.; Evans, J. E.; Ross, F. M. Electron-Beam-Driven Chemical Processes during Liquid Phase Transmission Electron Microscopy. *MRS Bull.* **2020**, *45* (9), 746–753. https://doi.org/10.1557/mrs.2020.227.

TABLE OF CONTENT ENTRY

